

# Peptide Programmed Hydrogels as Safe Sanctuary Microenvironments for Cell Transplantation

Yi Wang, Xuefei He, Kiara F. Bruggeman, Bishakhdat Gayen, Antonio Tricoli, Woei Ming Lee, Richard J. Williams,\* and David R. Nisbet\*

Cell transplantation is one of the most promising strategies for the minimally invasive treatment of a raft of injuries and diseases. However, a standing challenge to its efficacy is poor cell survival due to a lack of mechanical protection during administration and an unsupportive milieu thereafter. In response, a shear-injectable nanoscaffold vector is engineered considering the three equal requirements of protection, support, and survival. Here, the programmed peptide assembly of tissue-specific epitopes presents a safe sanctuary microenvironment for the transplantation of cells. For the first time, a mechanistic understanding of the multifactorial role of the nanoscaffold in promoting cell survival is presented, where initial cell survival is dependent on the fluid mechanic process of droplet formation rather than on shear rate. However, provided is the first report of the most critical component of a transplantation vector, distinguishing feigned biological support from mechanical properties from true ongoing biological support post transplantation. This is achieved via the presentation of amino acid constituents that significantly improve the efficacy of the vector compared to a biocompatible, yet inert analogue. Together, the peptide-programmed hydrogels enable fundamental rules for the engineering of advanced treatment strategies with wide reaching implications for tissue repair and biofabrication.

initial insult, but also as a result of a secondary injury which manifests as rapid necrotic death of cells and degradation of the local extracellular matrix (ECM) within the penumbra<sup>[2–4]</sup> This results in large, unstable, decellularised regions, which over time collapse and distort the surrounding tissue. This confounding factor autonomically inhibits regeneration across brain lesions within the adult mammalian central nervous system (CNS), thereby presenting a major neurological challenge for clinical treatments.<sup>[5]</sup> However, recent research into the potential of multicomponent, nanocellular and synthetic scaffolds<sup>[6]</sup> has shown the potential to integrate with the tissue to provide a biomimetic, synthetic ECM capable of filling voids.<sup>[3,7]</sup> This scaffold fulfills two critical functions: 1) mechanical support to avoid tissue distortion and collapse,<sup>[8]</sup> and 2) to provide a supportive milieu to endogenous and/or delivered replacement cells in the case of cell replacement therapy (CRT).<sup>[3,9]</sup>

CRT is a very attractive treatment option for neurological injury and disease, whereby replacement cells are grafted into the site of injury to regenerate and


repair the neural circuitry providing immediate symptomatic relief with longer term systemic repair.<sup>[10]</sup> Validation of the efficacy of CRT in the human brain has been clinically shown in Parkinson's disease patients. Fetal derived dopamine neurons have been transplanted into the striatum, with some patients

## 1. Introduction

Central nervous system lesions can arise due to a variety of reasons, including traumatic injury, disease, or infection.<sup>[1]</sup> Functional deficiencies, however, are not solely caused by the

Dr. Y. Wang, Dr. K. F. Bruggeman, Prof. D. R. Nisbet  
Laboratory of Advanced Biomaterials  
Research School of Electrical and Energy Engineering  
Australian National University  
Canberra, ACT 2601, Australia  
E-mail: david.nisbet@anu.edu.au

Dr. X. He, Dr. W. M. Lee  
Applied Optics Lab  
Research School of Electrical and Energy Engineering  
College of Engineering and Computer Science  
Australian National University  
Canberra, ACT 2601, Australia

 The ORCID identification number(s) for the author(s) of this article can be found under <https://doi.org/10.1002/adfm.201900390>.

Dr. B. Gayen  
Department of Mechanical Engineering  
University of Melbourne  
Parkville, VIC 3010, Australia

Prof. A. Tricoli  
Nanotechnology Research Laboratory  
Research School of Electrical and Energy Engineering  
Australian National University  
Canberra, ACT 2601, Australia

Dr. R. J. Williams  
Centre for Molecular and Medical Research  
School of Medicine  
Deakin University  
Warun Ponds, VIC 3216, Australia  
E-mail: richard.williams@deakin.edu.au

DOI: 10.1002/adfm.201900390

displaying symptomatic relief, evidence of transplanted cell integration within the host circuitry.<sup>[11]</sup> However, significant variability was reported in both the cell viability post administration and in functional recovery between patients.<sup>[12]</sup> Major variations in cell survival and innervation were observed within the host tissue, attributed, in part, to the nonconductive regenerative environment within the (damaged) adult brain.<sup>[13]</sup> This significant obstacle has resulted in these studies being abandoned with a large research effort instead focusing on the improving cell survival and reinnervation. During the direct injection of cells, (preferably via syringe administration to minimize iatrogenic injury), the cells experience a damaging shear regime, leading to mechanical membrane disruption and deformation, which accounts for a large percentage of cell death.<sup>[14]</sup> When cells are carried through the various media, they typically act like a passive tracer and are strongly influenced by the strain rate associated with the flow field.<sup>[15]</sup> In an effort to reduce such issues, and to improve reinnervation upon successful grafting of cells, we hypothesized that a rationally designed biomaterial scaffold that supported the cells during injection, and, once implanted, provided a safe sanctuary microenvironment for the cells, would improve CRT outcomes. These materials should be engineered to i) undergo a shear induced capillary flow, enabling injection and ii) mimic the native ECM with a highly hydrated nanofibrous structure, capable of providing the mechanical support and the biochemical signals required for cell adhesion and cellular functions, such as survival, migration and differentiation.<sup>[16]</sup>

Currently, electrospun nanofibers and a variety of hydrogels have been investigated to improve CRT due to their inherent characteristics, such as ease of production, biocompatibility, biodegradability, morphology, and chemical biofunctionalization.<sup>[17]</sup> Of these biomaterials, physical shear thinning hydrogels are among the most promising. These hydrogels present excellent shear induced flow characteristics to mechanically protect the cells, while also allowing minimally invasive administration with void filling capabilities.<sup>[17a,18]</sup> They are also highly hydrated, similar to physiological tissue, allowing rapid nutrient exchange and cell penetration,<sup>[17a,19]</sup> and subsequently providing a more favorable cellular milieu post administration.<sup>[20]</sup> Indeed, we have implanted such hydrogels within the brain and shown that they interface well with the surrounding parenchyma, reduce the associated inflammatory cascade, and encourage endogenous cell infiltration.<sup>[21]</sup> To achieve this, we previously pioneered the synthesis of biologically active and shear-thinning molecular hydrogels, and have investigated their utility as transplantation vectors for stem cells, demonstrating their ability to promote neural tissue repair and circuitry reconstruction in rodents, along with motor recovery.

Globally, we remain one of the few groups currently pioneering these short self-assembled peptide materials for this application, and as such there are many different aspects of the material that need to be further understood. Here, in order to better understand how our material has achieved the aforementioned results and to optimize the system further for translation, we have studied the dynamic properties of material that has previously only been studied in static form. We have demonstrated the capacity of this hydrogel as a transplantation vector to significantly increase cell survival by providing a

dynamically responsive, and mechanically protective micro-environment during cell transplantation. To gain insight as to the mechanism of cell protection we employed and validated a hydrodynamic fluid model, which allowed a detailed interrogation of the mechanism of mechanical protection during injection provided by self-assembling peptides (SAPs). We have demonstrated that the cells experience significantly reduced shear stress when embedded within these dynamically responsive hydrogels compared to administration as a suspension, the gold-standard delivery route. Interestingly, while it is accepted that shear causes cell membrane damage leading to cell death, our quantitative cell survival results between different fluids with different shear profiles demonstrate that the situation is not as straightforward. We suggest that cell survival may be more mechanistically dependent on the fluid mechanic processes of droplet formation (as opposed to continuous flow) than on the simple shear rate, as this threshold fluid behavioral observation correlated with the measured cell viability, yet a continuous correlation with changing shear rate was not observed. More importantly, we have also demonstrated the importance of the transplantation vector in providing a safe sanctuary milieu post administration, where we distinguished feigned biological support from mechanical properties of transplantation vectors from true ongoing biological support. This timeframe dependence of biological support has previously been a largely unexplored component of cell transplantation. We have now demonstrated that an improved cell transplantation vector should first increase viability during and immediately following administration; but second and most importantly (by comparison with an unfunctionalized yet mechanically similar analogue), we demonstrate that for therapeutic relevant cell survive postadministration it is imperative the transplantation vector provides a safe sanctuary milieu. This study provides clinically relevant guidelines for the rational design of multifunctional hydrogels to improve cell transplantation, in this case the direct injection of neural cells, to promote their Integration and long-term survival.

## 2. Dynamically Responsive Hydrogels as Vectors for the Direct Injection of Cells

Here, we used a previously developed dynamically responsive laminin-inspired hydrogel, designed to provide additional support to primary cortical neurons via the inclusion of a functional domain from laminin (Fmoc-DDIKVAV; referred to as Fmoc-Lam hereon), that spontaneously assembles to form a nanofibrous scaffold.<sup>[22–24]</sup> This was a deliberate target due to laminins being a major component of the neural stem cell niche,<sup>[25]</sup> with a demonstrated ability to influence stem cell maintenance, survival, differentiation and plasticity.<sup>[26]</sup> In order to demonstrate the need for the nanoscaffold to be optimized for the cell and tissue targets, we have also investigated two further epitope containing hydrogels; a Fmoc-FRGDF hydrogel that includes the functional domain from fibronectin, chosen as it can provide a neuroprotective role,<sup>[27]</sup> and coassembly of this system with Fmoc-Lam to present both RGD and IKVAV at equivalent density on the surface of the individual peptide fibers. Unlike the rationally designed Fmoc-Lam hydrogel, these two

systems are not “ideally” programmed for the specific cellular microenvironment of the cells deployed (here, primary cortical neurons as proof-of-concept), highlighting the clinical need to design the vector toward both the tissue and the cell type. The reason for this is that fibronectin is only presented in small quantities in the brain compared to laminin<sup>[28]</sup> and as our self-assembly mechanism presents very high density of the functional epitopes to the cells,<sup>[24]</sup> which in the case of RGD is not physiologically representative. As a further control, we have utilized the commercially available and structurally homologous, but nonpeptide containing, Fmoc-diphenylalanine (Fmoc-FF), which also presents as a dynamically responsive nanostructured hydrogel.<sup>[29]</sup> The chemical structures of each hydrogel are shown in **Figure 1A**. They both self-assemble through a conserved mechanism of molecular ordering of aromatic interactions ( $\pi$ - $\pi$  stacking) and hydrogen bonding to give similar nanoscaffolds (confirmation of higher order assembly to a consistent morphology is shown in Figure 1A and Figure S2, Supporting Information). The short peptide chains then assemble into supramolecular nanofibrils with external  $\beta$ -sheet domains (presenting the peptide sequence) and a hydrophobic core, that bundle into a hierarchical self-assembled nanofibrous network that is analogous in scale and morphology to the ECM found in vivo. The resultant hydrogels are transparent and self-supporting (Figure 1B (Fmoc-Lam and Fmoc-FF) and Figure S2A (Supporting Information) (Fmoc-FRGDF and co-assembled)). During cell transplantation, this dynamically responsive system protects the cells by redistributing the shear-forces away from the cell location. As a comparison, the gold standard transplantation of cells suspended in PBS was used with a schematic representation of cell administration depicted in Figure 1C.

The hydrogels were subjected to extensive characterization to confirm their structure and mechanical properties (Figure 1D–H, and Figure S2, Supporting Information). All four dynamically responsive hydrogels displayed no statistically difference in modulus and the same assembly mechanism (Figure S2E–H, Supporting Information). They also all presented as a highly porous, hydrated fibrous nanoscaffold suitable for deployment as a cell transplantation vehicle. However, while the Fmoc-FF system did present a nanofibrous morphology, it was different to the other, epitope laden hydrogels tested, with a statistically significant increase in fiber diameter ( $\approx$ twofold; Figure 1E,F) due to a ribbon like morphology. This is in agreement with other studies<sup>[29,30]</sup> and is discussed further below.

### 3. Dynamically Responsive Hydrogels Improved Cell Viability Postsyringe Injection

Next, we explored the cell-protective properties of the dynamically responsive hydrogels immediately upon administration using live/dead viability staining. Here, we have again used the gold standard transplantation of cells suspended in PBS to serve as our control.<sup>[31]</sup> After isolating primary cortical neurons, a concentration of  $10^7$  cells mL<sup>-1</sup> was prepared in PBS. This was mixed with the dynamically responsive hydrogels (or diluted further for the control) so that the final number of cells administered was  $5 \times 10^5$  cells. In the PBS only control

groups we observed that immediately following administration only  $\approx$ 75% of transplanted cells were viable (Figure 1I). In contrast, all of the dynamically responsive hydrogels that presented biologically active epitopes (Fmoc-Lam, Fmoc FRGDF, and their coassembly) achieved  $\approx$ 85% viability following injection. The Fmoc-FF hydrogel provided the best protection, with  $\approx$ 95% of the transplanted cells being viable. Although the hydrogel stiffnesses were not statistically different (Figure 1G and Figure S2, Supporting Information), TEM imaging reveals that while all SAPs formed an entangled nanofibrous network structure, the Fmoc-FF fibers had a broad ribbon like structure (Figure 1E), whereas the longer, more charged Fmoc-SAPs hydrogel yielded finer fibrils (Figure 1D,E and Figure S2B,C, Supporting Information). Considering it is on nanoscale dimension at which the bulk morphological differences occur, with a conserved microscale morphology, we do not expect them to influence cell viability during injection through a syringe. On further investigation, it appears that it is the gelation kinetics which is the critical parameter. We explored the gelation recovery times post-removal of shear stress for all of the hydrogels (Figure 1G,H). Statistically, only the Fmoc-FF group showed a difference from the other hydrogel groups, recovering much more rapidly (104 and 870 s for the Fmoc-FF and Fmoc-Lam hydrogels respectively; Figure 1H). Each of these systems is governed by the same basic molecular rules, meaning each is shear reversible (Figure 1G), and they have similar shear thinning kinetics (Figure S2D, Supporting Information). However, Fmoc-FF was designed solely to assemble as efficiently as possible, and as such recovers much more rapidly into a robust nanoscaffold upon shear removal, meaning it can mechanically support administered cells more rapidly. Conversely, the epitope containing hydrogels are a compromise between stability and incorporating and presenting sequences that enable functionalization.<sup>[22]</sup> This difference in gelation kinetics explains the improved protective capacity of the Fmoc-FF system immediately following administration and as such, when considered only via this parameter, is superior. However, these results indicate that irrespective of functionalization, all four of the dynamically responsive hydrogels provided mechanical protection during transplantation, thereby protecting the cells from the severe shear stresses that arise from the flow regime during administration. However, it is clear when engineering for transplantation vectors, faster in situ gelation times are desirable.

### 4. Long-Term Cell Viability Postsyringe Injection

All of the dynamically responsive hydrogel systems offered superior protection upon direct injection compared to control, thereby satisfying the first requirement of a CRT (i.e., a vector to offer mechanical protection from shear). Importantly, the commercially available Fmoc-FF hydrogel outperformed all three of our rationally designed biologically relevant hydrogels due to its more rapid gelation recovery, but all four systems showed increased viability immediately following administration. Next, we wished to explore the long-term effects (defined here as 5 d cultures) of concomitant administration of cells with our dynamic hydrogel on long-term cellular outcomes. This was necessary for realizing the second requirement of

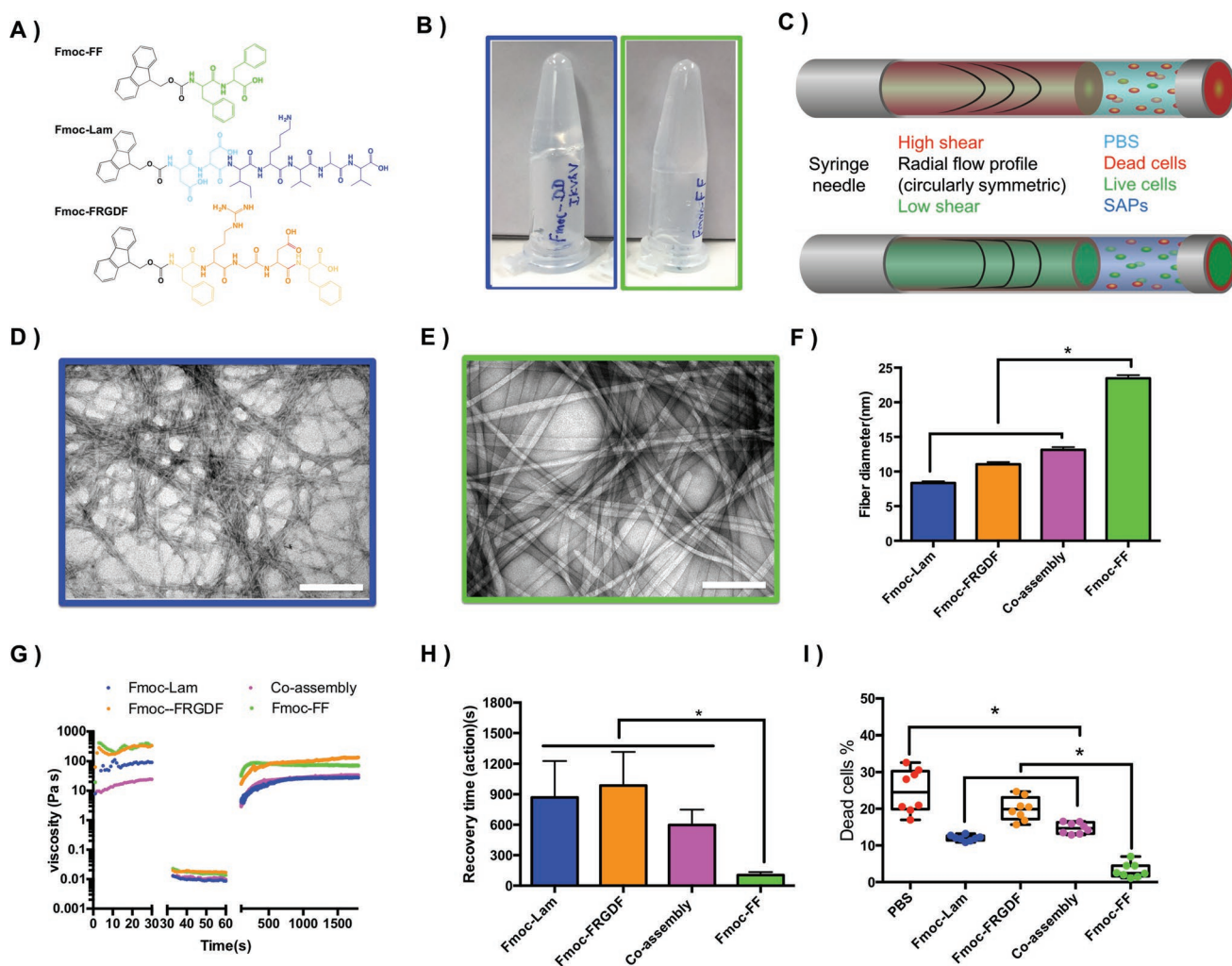


**Figure 1.** A) Shows the chemical structure of peptides hydrogels tested (Fmoc-FF, Fmoc-Lam, Fmoc-FRGDF), with the coassembled system consisting of a 1:1 ratio of Fmoc-Lam and Fmoc-FRGDF. B) An inversion test of the Fmoc-Lam (left, blue) and Fmoc-FF (right, green) hydrogels formed after a pH switch. C) A schematic representation of cell injection with the dynamic responsive hydrogel and, as a comparison, the gold standard administration route (i.e., cells in suspension methodology). Unlike the standard methodology (PBS or media), the dynamically responsive hydrogel protects the cells by redistributing the shear-forces away from the cell location. D,E) Representative TEM images of Fmoc-Lam and Fmoc-FF, respectively. F) Quantitative data comparing the nanofiber diameter obtained from TEM imaging of Fmoc-Lam (blue), Fmoc-FRGDF (orange), coassembly (magenta), and Fmoc-FF (green), respectively. There was no statistical difference between the nanofiber diameters of any of the hydrogels that included biologically active epitopes. The Fmoc-FF system had statistically larger fibers due to the ribbon fiber structures formed during its assembly. G) Characterizes the recover of the shear thinning hydrogels upon removal of shear. This was achieved by applying a shear rate at  $0.01 \text{ s}^{-1}$  for 30 s, then applying a shear rate at  $792 \text{ s}^{-1}$  (which matches the average of strain rate of hydrogel) for 30 s, before finally applying shear rate at  $0.01 \text{ s}^{-1}$  for 30 min to determine the recovery kinetics of the SAP hydrogel; H) Recovery time of the different hydrogel systems, showing Fmoc-FF had the most rapid recovery of 104 s, with Fmoc-Lam taking 870 s; I) Shows the percentages of dead cells postdirect injection. This highlights that irrespective of functionalization within a laminin epitope, all dynamically responsive hydrogels provided mechanical protection during transplantation, by reducing the exposure of encapsulated cells to the severe shear stresses that arise from the flow regime during administration, and that Fmoc-FF has the least percentage of dead cell. \* represent  $P < 0.05$ . Scale bars represent 200 nm.

CRT: enabling the regenerative potential of transplanted cells. Therefore, to examine the survival and maintenance of transplanted cells administered within our dynamically responsive hydrogels, we cultured injection administered primary cortical neurons out to 5 d, using an administration density of  $2.5 \times 10^6$  cells  $\text{well}^{-1}$ .

As expected, we observed negligible cell death on the 2D PDL controls in long term culture (Figure 2A). This was due to the initial cell death that was caused during administration (i.e., the initial 75% viability postinjection reported above).

Unable to attach to the PDL surface postadministration, the initial dead cells were undetectable during the 5 d study. Importantly, in our long-term cultures where cells were administered within the vector Fmoc-Lam, no reduction in cell viability was observed postadministration (Figure 2B,C,E). This was a significant result, validating our dynamically responsive hydrogel as a cell transplantation vector, as the dead cells that were present immediately upon administration remained entrapped within the hydrogel upon spontaneous self-assembly, and hence were detected at the 5 d timepoint. This indicates that there was no

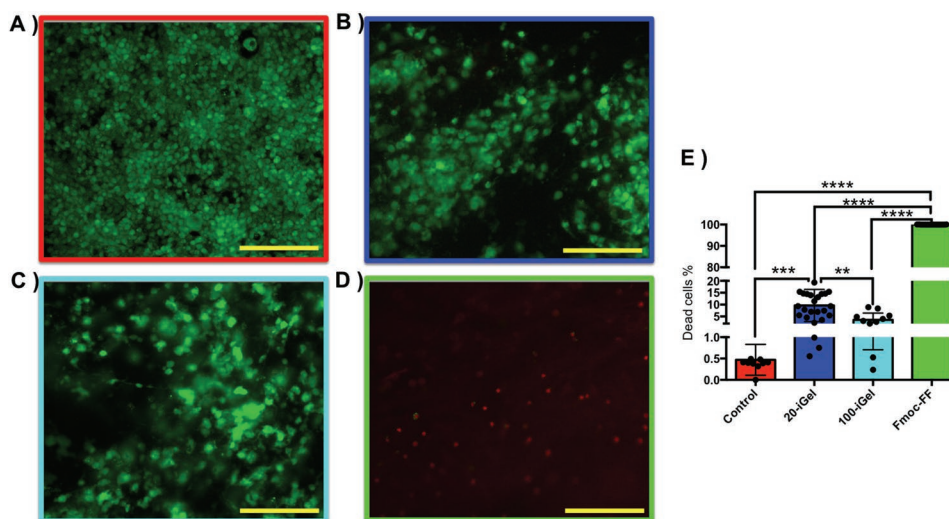


**Figure 2.** Representative fluorescence images of primary cortical neurons at high cell density for long-term cell viability (5 d) postsyringe injection. A) the PDL control B,C) Postinjection of mixing cells and Fmoc-Lam hydrogel (total volume of injection: 20 and 100  $\mu$ L, respectively) on the Fmoc-Lam hydrogel, D) Fmoc-FF hydrogel, E) Percentages of dead cells post injection for long-term culture (5 d) at the high density of cells in groups: PDL control, 20-iGel (20  $\mu$ L of Fmoc-Lam), 100-iGel (100  $\mu$ L of Fmoc-Lam), and Fmoc-FF. \*\*, \*\*\*, and \*\*\*\* represent  $P < 0.01$ ,  $P < 0.001$ , and  $P < 0.0001$ , respectively. Scale bars represent 100  $\mu$ m.

further cell death postadministration in long-term culture, validating that the presented amino acid constituents within our dynamically responsive hydrogel provide a bona-fide safe sanctuary milieu for transplanted cells.

In contrast, no viable neurons were observed on the commercially available Fmoc-FF dynamically responsive hydrogel (Figure 2D,E). Therefore, we have demonstrated in long-term culture that our fully defined laminin based molecular hydrogel provides a static and stable microenvironment postdynamic cell transplantation that significantly increases long-term cell survival. While both hydrogels (Fmoc-Lam and Fmoc-FF) significantly enhance cell survival immediately after dynamic cell administration by providing mechanical protection and redistribution of shear forces, only functionalized Fmoc-Lam supported post injection cell survival. This has allowed us to distinguish between feigned biological support (support offered by the hydrogels immediately following transplantation) that is dominated by the mechanical properties of the transplantation vector from true ongoing biological support posttransplantation. These results highlight the importance of the presentation of relevant biological signals and their temporal dependence, in addition to the mechanical and morphological cues found in the native ECM to provide a safe sanctuary microenvironment for the long-term maintenance of transplanted cells. For instance, here we rationally designed the peptide hydrogel to include the laminin-based epitope IKVAV. This is due to the system i) fully synthetic (as opposed to whole protein inclusion), ii) the epitope has been shown to promote neuronal adhesion and differentiation,<sup>[32]</sup> and iii) presents more efficiently than the entire laminin protein due to the increased density of its presentation on the peptide fibril.<sup>[33]</sup>

We have clearly demonstrated that a combinatorial strategy is essential to improve the efficacy of current cell transplantation technologies, as simply protecting cells during administration does not guarantee long-term cell survival. The Fmoc-FF system

was statistically superior immediately post-injection, but it is not clinically relevant as it does not satisfy both requirements of a CRT material with no viable cells being detected after 5 d of in vitro culture.

Next, we wanted to investigate our dynamically responsive hydrogel as a transplantation vector further to understand the relationship between the density of transplanted cells within the hydrogel and their long-term viability. Here, we employed two different hydrogel volumes (20 and 100  $\mu$ L) that both contained  $2.5 \times 10^6$  cells to determine the effect of cell density on viability (Figure 2B,C,E). In the 20  $\mu$ L hydrogel sample, a slight increase in cell death from  $3.6 \pm 2.8\%$  in 100  $\mu$ L hydrogel to  $9.6 \pm 6.7\%$  was observed. However, while this indicated that decreased density may be appropriate to improve cell survival upon administration within the Fmoc-Lam hydrogel (Figure 2E), as discussed above there is a second requirement regarding the presentation and availability of relevant biological signals to promote long-term survival. Furthermore, we hypothesize that at higher densities, it is likely that nonapoptotic cell shedding occurs caused by cell overcrowding.<sup>[34]</sup> This means that there will be an optimal cell density within a transplantation vector that is highly dependent on the individual hierarchical properties of the nanoscaffold and the cell phenotype delivered, where lower densities are insufficient for appropriate cell-cell interactions result in death, as does overcrowding at higher densities.

To further examine this effect, long-term cultures were performed at further decreased cell density ( $1.0 \times 10^5$  cells well<sup>-1</sup>) on top of each hydrogel. Importantly, we have shown in such cultures that cells will actively and extensively infiltrate these molecular hydrogels.<sup>[35]</sup> Cells were plated on top of a preformed hydrogel to ensure that once seeded on the control and the top of our 3D hydrogels that the cell distribution and density were the same, i.e., the tendency of cell–cell communication on the hydrogel and PDL control was controlled. However, as cells infiltrated the 3D scaffold, the tendency for supportive cell–

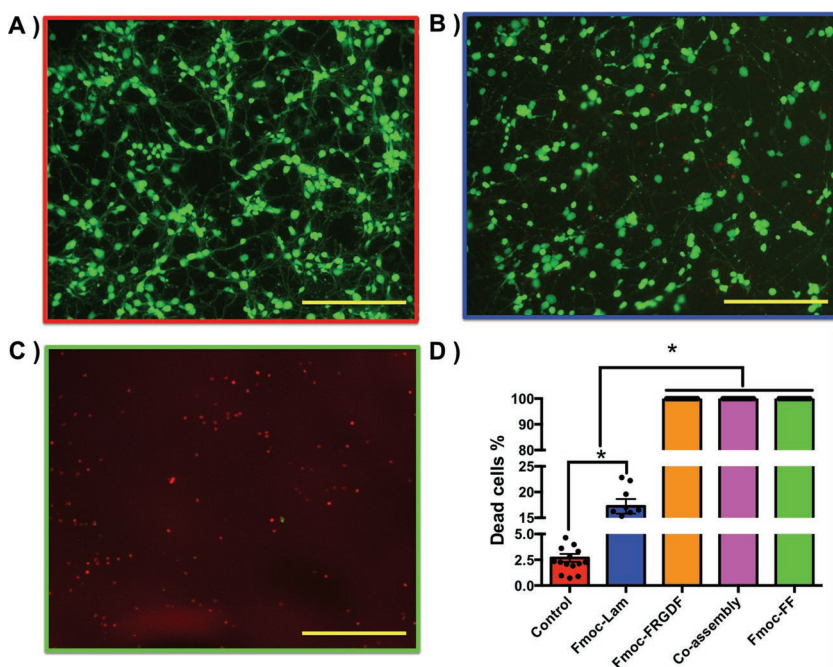


**Figure 3.** Representative fluorescence images of primary cortical neurons at a decreased cell density for long-term cell viability (5 d) postsyringe injection. Importantly, cells were deliberately plated on top of a preformed hydrogel to ensure that once seeded on the control and the four hydrogel groups that the cell distribution and density were the same immediately upon plating. This was designed to ensure that the tendency of cell–cell communication on the hydrogels and PDL control were to same initially before cells began to infiltration the hierarchical 3D scaffolds. A–C) PDL control, Fmoc-Lam, and Fmoc-FF, respectively (noted that only an image of Fmoc-FF is represented as the Fmoc-FRGDF and coassembled systems also showed 100% death); D) Percentages of dead cells on SAPs hydrogels post 5 d and control group. \* represents  $P < 0.05$ . Scale bars represent 200  $\mu\text{m}$ .

cell interactions to occur would reduce. Again, the Fmoc-FF hydrogel, and both hydrogels presenting the RGD epitope had detrimental effect on neuronal survival, which is attributed to a lack of biologically active sequences to support cells (Figure 3C) as reported above. We have previously reported that RGD is not an optimal epitope to support neurons as fibronectin is not abundantly present within the brain,<sup>[36]</sup> which is further supported here. When culturing cells at the decreased density, we observed 14.5% cell death in the Fmoc-Lam hydrogel, showing an increase compared to the 2D PDL control group where the reported cell dead was  $\approx 2.7\%$  (Figure 3A,B,D). This increase in cell death on the dynamically responsive hydrogels highlights the importance of appropriate cell density to facilitate cell–cell interaction/communication in long term cultures, which is particularly relevant when moving from a 2D surface to a highly porous 3D scaffold with significantly greater surface area. We suggest that this results from the significant increase in surface area, requiring significant cellular secretion of paracrine trophic factors to support viability and development of synaptic interactions and connections<sup>[37,38]</sup> and at decreased cell density the cells are too widely dispersed to provide such support. Therefore, from this study it is inferred that when optimal transplantation densities are unknown (clinically, this is the most likely scenario), higher transplantation densities are optimal, even considering cell overcrowding effects. This has other implications, particularly in cell transplantation. There-

fore, this system, with its ability to expand cell numbers *ex vivo*, presents further advantages for its use.

In this case, the dynamically responsive hydrogels were shown to be capable of offering mechanical protection during administration, while also promoting the long-term survival of transplanted cells post administration when the cell concentration was  $2.5 \times 10^7 \text{ cell mL}^{-1}$  in the Fmoc-Lam vector.

## 5. Hydrodynamic Fluid Model for Flow through a Small Gauge Needle

Having determined that cell administration and long-term culture within our dynamically responsive hydrogel resulted in significantly improved cellular outcomes, we explored the mechanism for this phenomenon. Here, we wished to confirm the expected shear thinning profile in our SAP gels validated the discussion of shear rates within the respective fluids to understand how this profile influences cell survival. While it is accepted that shear causes cell membrane disruption and subsequently death during needle administration, our quantitative cell survival results in different fluids with different shear profiles to demonstrate that the situation is not straight-

forward (discussed further below). We empirically confirmed a hydrodynamic fluid model of the cell administration in SAP hydrogels, and utilized the theoretical model to probe the reason for the observed increase in cell viability immediately following administration for the SAP hydrogels compared to cells delivered in PBS.

In the present experiment, a flow rate  $Q$  ( $=1 \text{ mL min}^{-1}$ ) was maintained during administration. The decrease in diameter from syringe to needle ( $D_{\text{syringe}}/D_{\text{needle}} = 9.4$ ) results in an increase in average flow velocity of the medium in the needle by a factor of  $D_{\text{syringe}}^2/D_{\text{needle}}^2$  ( $\approx 88.36$ ). For this reason, cells would experience greater strain inside the needle bore compared to the syringe, and subsequently be vulnerable to damage and even death under this hydrodynamic force. Furthermore, the strain rate is dependent on the viscosity of the medium,<sup>[15]</sup> hence when utilizing hydrogels as a replacement for media that is typically used for cell transplantation there will be a significant difference in the hydrodynamic forces that must be understood and optimized. Here we have used two different mediums: PBS, treated as a Newtonian fluid with a constant viscosity similar to cell culture media, and our Fmoc-Lam hydrogel, which behaves like a time independent non-Newtonian fluid. To obtain the strain rate field, we used an intuitive fluid model as described in Figure S3 (Supporting Information). Under our experimental conditions, the Reynolds number (which is defined as the ratio between the inertia and viscous force) of the

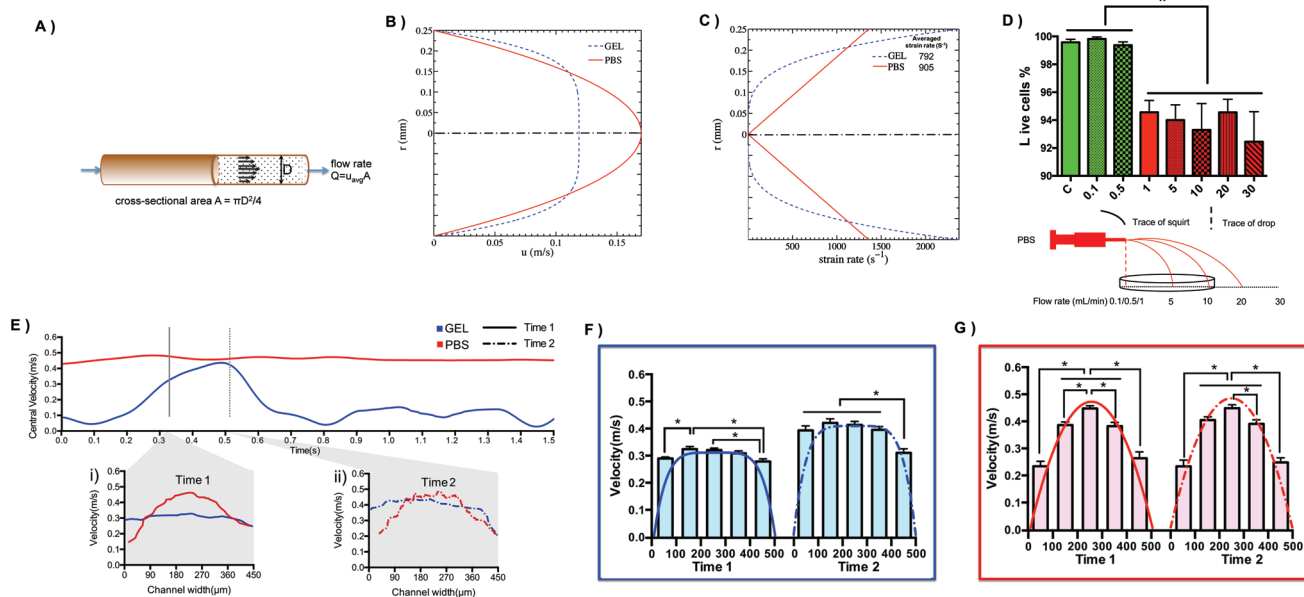


**Figure 4.** Shows the flow characteristics of PBS and our Fmoc-Lam hydrogel in a hydrodynamic fluid model. A) Fully developed flow through the portion of the Terumo needle of diameter  $D = 0.5$  mm and flow rate  $Q = 1$  mL min<sup>-1</sup> along with cross-section of the needle bore; B) Laminar velocity profiles of axial velocity,  $u$  (m s<sup>-1</sup>), for two media as function of distance,  $r$  (mm) from the central line (shown as dash-dotted line) of the needle bore; C) the distribution of the strain rate ( $s^{-1}$ ) over the cross-sectional area and averaged strain rate for two media (hydrogel and PBS) where averaging is done over circular extending from the central line; D) Percentage of live cells postinjection in PBS at varied flow rate (0.1, 0.5, 1, 5, 10, 20, 30 mL min<sup>-1</sup>) and their respective flow traces where ejection distances were quantified and have been shown schematically; E) experimental velocity data obtained from custom designed microfluidic chip. Central velocities for the hydrogel and PBS during injection (data smoothed with second order of smoothing polynomial and 6 neighbors to average on each size); i) and ii) velocity profiles every 100  $\mu$ m across the channel at Time 1 (with an average velocity) and Time 2 (with high velocity), indicated by line and dash line, respectively. The data were smoothed with nine neighbors to average on each size. F) Microfluidic velocity data of the hydrogel's velocity profiles at Time 1 and Time 2. G) Microfluidic velocity data of PBS's velocity profiles at Time 1 (with average velocity) and Time 2 (with high velocity).

flow was small, and flow remained laminar inside the needle as shown in Figure 4A,B. The fully developed laminar velocity profile,  $u$  (m s<sup>-1</sup>), for the PBS medium was parabolic, whereas the profile became flattened for the hydrogel (Figure 4B), which is characteristic for shear thinning fluids.<sup>[15]</sup> In both cases, the velocities peaked at the central line and were zero at the bore wall. Profiles of the strain rate as a function of distance from the central line,  $r$ , for each medium are illustrated in Figure 4C. PBS shows a linear variation of the strain rate over the cross-section with a maximum shear rate of 1358.1 s<sup>-1</sup> at the wall of the needle bore, and an average across the cross-sectional area of 905.4 s<sup>-1</sup>. Though the maximum strain rate for the hydrogel was much larger than that of PBS, lower values of strain rate persist over a significant portion ( $\approx 80\%$  by diameter,  $\approx 64\%$  by area) of the bore cross-section, with an average strain rate of only 792 s<sup>-1</sup> across the cross-sectional area (a 12.5% reduction from PBS) as shown in Figure 4C. These hydrodynamic fluid models concur with our experimental data, predicting that the cells experience lower strain rate in the hydrogel medium (i.e., the hydrogel provides mechanical protection), resulting in enhancement of the cell viability compared to PBS (the current state-of-the-art for cells replacement technology). Importantly, we believe that there may be multiple mechanisms at play and the effects we observed of cell viability did not correspond to a proportional linear relationship between shear rate and cell death, instead, and interestingly, we observe a threshold effect (discussed further below).

## 6. Experimental Velocity Data for Validation of the Hydrodynamic Fluid Model

Validation of the model was pursued using a microfluidic setup to simulate the cell administration process using polystyrene microspheres as cell substitutes. Not surprisingly, excellent agreement between the hydrodynamic fluid model and the microfluidic data validates the theoretical model, confirming that SAP hydrogels can be modeled as time independent non-Newtonian fluids.

During administration, we captured video sequences (150 fps) of microspheres flowing in our channels. The exposure time (ET) for each frame was 0.2 ms. Here, we define the central velocity as the velocity of the spheres in the middle of the channel during administration. The velocity profile was determined as the velocity of all spheres captured during an exposure. Figure 4E shows the central velocities, an average of the velocities of spheres that were located within  $250 \pm 50$   $\mu$ m from the channel edge. The central velocity for the PBS was observed to be constant during the administration time course, while the central velocity of hydrogel showed fluctuation. Our dynamically responsive hydrogels have been engineered to be shear thinning; the physical bonds forming crosslinking points within the hydrogel network are reversible, and can be broken by the application of shear stress to allow the material to flow easily.<sup>[39]</sup> Rapid recovery is observed after removal of shear, where the supramolecular fibrils are able to re-establish

connections to form the hydrogel (Figure 1G,H).<sup>[40]</sup> Upon application of flow, a low-viscosity region of hydrogel was established, visualized by a constant, high velocity of the reporter spheres. However, a low velocity region was also observed at different time points during administration. We suggest that the high velocity region contributes to the shear induced solution phase while the relative low velocity contributes to a slow moving, hydrogel phase.

To further characterize the velocity profiles across the channel, we studied two different time points during administration. It is important to note that it was not possible to analyze spheres close to the bore wall hence the velocity discrepancies in this region could not be experimentally observed. However, the flat region (region of constant strain) within the velocity profiles for the hydrogel occupies 80% of the entire width of the channel. Figure 4E–G shows the velocity profiles within the hydrogel and PBS. The plots confirm our hydrodynamic fluid model showing that velocity profiles of PBS at two time points display parabolic profiles, while again similar to our model the profiles of the hydrogel are more uniform across the channel albeit with different offsets. Since the velocity of the hydrogel is identical within these regions across the channel, the velocity gradient within the hydrogel is much smaller than for PBS administration. For this reason, most cells encapsulated within the hydrogel are mechanically protected from the shear force compared with cells in PBS, which is consistent with the strain rate plot of the numerical model (Figure 4C) and our experimental neuronal cell transplantation data. A combination of the experimental velocity data with our numerical model is shown in Figure 4F,G for our dynamically responsive hydrogel and PBS respectively. Overall, the numerical model shows good agreement with the experimental data. Importantly, for future optimization studies there is inherent flexibility in the current experimental model, such as the tunability of the stiffness of the PDMS that can also alter the shearing effects close to the interface that can be tailored to suit other needle materials such as polymeric microneedles.<sup>[41]</sup>

While we have shown that shear stress close to the walls of the syringe is high, and shear stress is known to be capable of cell membrane disruption, we contend that the effects we see do not correspond to a proportional linear relationship between shear rate and cell death. We conducted further investigation in PBS with increasing flow rates to further understand the influence of shear rate on cell death where we observed a threshold effect on cell survival (Figure 4D). Even a threshold value of survivable shear forces would be expected to show as a continuous relationship with cell viability as the non-constant shear profiles mean that proportion of fluid under the threshold would vary continuously. In a further exploration of the mechanics and flow properties, we found cell survival to correlate to the transition when the kinetic energy of the flowing solution overcomes its surface energy, distinguishable by continuous flow and fluid ejection from the needle, as opposed to droplet formation (shown schematically in Figure 4D). When flow is increased the shear rate is increased, but more importantly the fluid begins to be ejected from the needle. This property correlates with the threshold of reduced viability we observed shown in Figure 4D, where at flows of  $>1 \text{ mL min}^{-1}$  the fluid is ejected from the needle. Interestingly, this is a threshold effect

and when the fluid has more kinetic energy at  $30 \text{ mL min}^{-1}$  and is ejected further (shown in Figure 4D, where the ejection distances were quantified) there was no further decrease in cell death supporting the conclusion that the effects on cell viability do not correspond to a proportional linear relationship between shear rate and cell death. Importantly, this further supports the conclusion that when engineering a transplantation vector, the most critical component is the provision of vital biological support post administration, rather than a focus on improving cell viability as they travel through a needle.

In summary, we present a design for a multifunctional peptide-based hydrogel as a transplantation vector to greatly improve the fate of cells administered to damaged tissue. A noncovalent nanoscaffold was engineered by the self-assembly of functionalized peptide derivatives at physiological pH (7.4), to provide an injectable, dynamically supportive material for the protection of cells during administration, as well as an optimal microenvironment for their growth. We have demonstrated their efficacy as a delivery vehicle for cell transplantation technology, increasing the survival of injected cells. In order to identify the critical design parameters for optimal function, we have developed a predictive model to provide critical insight when engineering or further optimizing cell transplantation vectors. First, hydrodynamic fluid modeling was used, theoretically providing a mechanistic understanding of cell protection provided by the hydrogel during administration. Similarly, the velocity of cell proxy microspheres during simulated cell transplantation was tracked, which validated the proposed numerical model and to greater extent demonstrated the potential of the nanofibrous hydrogel as a mechanically beneficial injectable delivery vector. However, our study also suggests that cell survival may be more mechanistically dependent on the fluid mechanics governing the process of droplet formation (as opposed to continuous flow) than on the simple shear rate, as this threshold fluid behavioral observation correlated with the measured cell viability. The full mechanism of cell death and cell protection during needle flow remains unknown, and this manuscript provides new quantitative insight to direct further investigations. However, we now know that this is not the most vital function performed by a delivery vector; rather the ongoing biologically supportive parameters provided and their temporal dependence in influencing cell survival and growth must be considered and optimized. We have demonstrated that multiple requirements are essential when engineering vectors for cells transplantation: firstly, that the vector should increase viability during and immediately following administration as much as possible; but second and most importantly, (by comparison with an unfunctionalized yet mechanically similar analogue) we demonstrate that postadministration the transplantation vector must provide a safe sanctuary milieu, here achieved by peptide programming to reflect the specific cellular microenvironment of the tissue being repaired (in this case, the brain as proof-of-concept). We suggest, based on the studies presented here, that the latter of these factors is the most vital consideration to ensure the therapeutic cells can survive and function; hence our hypothesis suggests that a transplantation vector must be specifically engineered the precisely mimic the (healthy) cellular microenvironment of its intended deployment. Overall, our specifically engineered dynamically responsive system protects

cells during and postsyringe administration and supports their long-term survival. The approach of presenting biologically relevant epitopes within a dynamically responsive hydrogel has far reaching material applications, including as vectors for the administration of regenerative stem cells.

## 7. Experimental Section

**Animals and Materials:** All reagents and animals used in this study were commercially available. All animal procedures and methods were conducted in accordance with the Australian National Health and Medical Research Council's published Code of Practice for the Use of Animals in Research and were approved by the ANU Animal Care and Use Committee (animal ethics protocol: A2013/41).

Fmoc-protected amino acids, hydroxybenzotriazole (HOBt), O-benzotriazole-*N,N,N'*,*N'*-tetramethyl-uronium-hexafluoro-phosphate (HBTU) and Wang based resins were purchased from GL Biochem (China), and all other chemicals were purchased from Sigma-Aldrich (USA).

Tissue culture polystyrene culture plates (TCP) were purchased from NUNC Inc., Denmark. All primary cortical neurons reagents were purchased from Gibco except for gentamicin from Sigma.

**Preparation and Characterization of Fmoc-SAPs Hydrogel:** Fmoc-SAPs were manually synthesized via solid phase peptide synthesis (SPPS) as previously described.<sup>[42]</sup> SPPS was carried out in a rotating glass reactor vessel at a 0.4 mmol scale. Specifically, synthesis involves stepwise deprotection and coupling of bead resin-attached amino acid (AA) (e.g., Fmoc-lys (Boc)-Wang resin). Deprotection was carried out in 20% piperidine in DMF for 20 min. Subsequent amino acid residues were then incorporated via the addition of a coupling solution consisting of an excess of the required Fmoc-protected amino acid (2 mmol), HBTU (1.92 mmol, 720.00 mg), HOBt (2.00 mmol, 272.00 mg), *N,N*-diisopropylethylamine (DIPEA) (4.8 mmol, 0.80 mL) and 8 mL DMF, and mixed via stirring for 60 min. After the final coupling step, the resin was washed with ethanol and dried under the constant vacuum over for 48 h. A Kaiser test was used for the detection of free amines to confirm the success of each deprotection and coupling step.

After drying, the Fmoc-SAP was cleaved from the resin using trifluoroacetic acid (TFA) with 2.5% distilled water and 2.5% triethyl silane (TES) for 2 h with shaking every 30 min. The solution was then filtered through glass wool to remove the resin, before excess TFA was removed by nitrogen sparge until the final volume of solution reduced to less than 5 mL. The solution was then precipitated in cold ether, centrifuged and the collected powder placed under constant vacuum for 7 d.

**Fmoc-SAP Hydrogel Formation:** All hydrogels were prepared to a final concentration of 15 mg mL<sup>-1</sup>. Briefly, 10 mg of peptide was dissolved in 100  $\mu$ L of deionized water with 50  $\mu$ L of 0.5 M sodium hydroxide (NaOH). Then 0.1 M of hydrochloric acid (HCl) was added dropwise with continuous vortexing, until the solution reached physiological relevant pH (Oaktron pH 700 micro pH electrode, Thermo Scientific). Once the PBS was added to bring the gel up into 15 mg mL<sup>-1</sup> concentration. For in vitro cell work, Hank's buffered saline solution (HBSS) (Gibco) was used in place of the PBS. Hydrogels (350  $\mu$ L well<sup>-1</sup> for 24-well plate) were loaded into wells after sterilization by ultraviolet (UV) lamp for 2 h, and PBS/HBSS was added on top of hydrogel for 24 h and stored in the incubator (37 °C, 5% CO<sub>2</sub>) prior to cell seeding to equilibrate. For control, cells were cultured on poly-D-Lysine (PDL)-coated coverslip without hydrogel.

**Rheology:** The rheological analysis was performed using a Kinexus Pro+ Rheometer (Malvern). Approximately 0.2 mL of hydrogel sample was placed on a 20 mm roughened plate (with solvent trap, Lower Geometry: PLS55 C0177 SS, Upper Geometry: PU20 SR1351 SS). The gap size was 0.2 mm, and multiple frequency sweeps were performed for frequencies ranging from 0.1–100 Hz with a 0.1% oscillatory strain at a constant temperature of 25 °C.

A linear shear rate sweep from 0.01 to 100 s<sup>-1</sup> was employed to characterize the shear thinning kinetics of the hydrogel. Shear-thinning

and reassembly experiments were performed by applying a shear rate at 0.01 s<sup>-1</sup> for 30 s, then applying a shear rate at 792 s<sup>-1</sup> (which matches the average of strain rate of gel) for 30 s, and finally applying shear rate at 0.01 s<sup>-1</sup> for 30 min to determine the recovery kinetics of the SAP hydrogel.

**Fourier Transform Infrared Spectroscopy (FTIR):** FTIR was performed to monitor the interactions in the Amide I region (1550–1750 cm<sup>-1</sup>) using an Alpha Platinum Attenuated Total Reflectance (ATR) FTIR (Bruker Optics). Approximately 30  $\mu$ L of sample hydrogel was placed on the single reflection diamond and absorbance scans were obtained for each peptide, and a background buffer scan subtracted.

**Circular Dichroism:** Circular dichroism was used to determine secondary structure using a Chirascan CD Spectrometer (Applied Photophysics Limited). The hydrogel was diluted 1/100 with DiH<sub>2</sub>O to reduce scatter. The diluted gel around 400  $\mu$ L was added into the cuvette with a 10 mm pathlength. CD scans from 180 to 320 nm with a step size of 0.5 bandwidths and a baseline (DiH<sub>2</sub>O) was subtracted. The resulting data were averaged and smoothed postacquisition using software provided by Chirascan prior to analysis.

**Transmission Electron Microscopy:** Negative stain transmission electron microscopy (TEM) was performed on a Hitachi H7100FA electron microscope with a LaB6 cathode at 100 kV. Formvar-coated copper grids were prepared with electron glow discharge at 15 mA for 30 s, observing a purple plasma bloom. The formvar-coated side of the grid was applied to the hydrogel sample for 30 s, was washed with water (20  $\mu$ L), then treated with 1 drop of UF (20  $\mu$ L) and finally immersed into UF drop for 30 s, blotting off the excess solution using filter paper between each step. The grids were then stored overnight before imaging for TEM. We have validated this methodology for the Fmoc-hydrogels using cryo-TEM,<sup>[43]</sup> the Fmoc-DIKAV hydrogel with atomic force microscopy<sup>[22,36]</sup> and subsequently for even weaker gels (<100 Pa) with both AFM, SANS, and SAXS<sup>[24,44]</sup> analysis showing the morphology to be reflective of the TEM analysis.

**Mouse Primary Cortical Neuron Culture:** The culture plates were treated with 10  $\mu$ g mL<sup>-1</sup> of poly-D-lysine (PDL) coating and placed in an incubator overnight. Next day, culture plates were washed three times with PBS to remove PDL and were stored for use.

Isolation and culture of primary cortical neurons was performed as previously described<sup>[45]</sup> unless otherwise noted. Briefly, mice were attained from Australian Phenomics Facility (APF) by time-mated overnight and a vaginal plug on the next morning (as the embryonic day E 0.5) for embryo collection at E14.5. Then, the pregnant mouse was sacrificed by cervical dislocation (CD) and E14.5 fetuses were collected, and cortical dissection for cortices without hindbrain, olfactory bulb and meninges was performed under sterile conditions. The cortices were trypsinized for 20 min in the incubator (37 °C, 5% CO<sub>2</sub>) in Hank's balanced salt solution (HBSS) (Invitrogen) with 1  $\times$  0.25% trypsin (Gibco), 1x DNAase (Gibco). After digestion, cells were washed three times with HBSS. Minimum essential medium (MEM) solution with 10% fetal bovine serum (FBS) was added to dissociated tissue into dispersed cells and counted with a hemocytometer and trypan blue exclusion for use. The desired cell density was loaded into the culture plates. For high and low cell density experiments, cells were seeded at 5  $\times$  10<sup>6</sup> cell mL<sup>-1</sup> and 2  $\times$  10<sup>5</sup> cell mL<sup>-1</sup> respectively to obtain 2.5  $\times$  10<sup>6</sup> cells well<sup>-1</sup> and 10<sup>5</sup> cells well<sup>-1</sup>. After 2 h attachment, primary culture media containing Neurobasal medium (Gibco), 1% B27 serum-free Supplement (Gibco), 5  $\times$  10<sup>-3</sup> M glutamine (Gibco) and 10  $\mu$ g mL<sup>-1</sup> gentamicin (Sigma) was used to replace the old medium for 5 d culture.

**Cell Administration via Syringe Injection and Quantification of Viability:** **Cell Viability Postdirect Needle Injection:** Cell injections were carried out via the needle/syringe injection. Briefly, 450  $\mu$ L gel mixed with 50  $\mu$ L cells (5  $\times$  10<sup>5</sup> cells per 50  $\mu$ L) which modified on the previous description.<sup>[16d]</sup> Briefly, the hydrogel was vortexed for 1 min and then load cells into the hydrogel while it is in a liquid state. The mixture rapidly reforms into a hydrogel when shear is removed (these kinetics are shown in Figure 1). All cells are encapsulated in gels, which we refer to as cells cultured in 3D. The mixture was injected into a coverslip plate by syringe fitted with 25G Terumo needle with flow rate (1 mL min<sup>-1</sup>) by a syringe pump ( $D_{\text{syringe}}/D_{\text{needle}} = 9.4$ ). This flow rate was selected as it matches

the maximum flow rate employed in our rodent stroke and Parkinson disease models, where cells were administered through a 100  $\mu\text{m}$  Hamilton Syringe. Interestingly, it also corresponded to the threshold effect observed in cell viability between 0.5 and 1  $\text{mL min}^{-1}$  for the 25G needle deployed in this study. To investigate the effect of flow rate on cell survival, the flow rate was varied between 0.1, 0.5, 1, 5, 10, 20, 30  $\text{mL min}^{-1}$ . Cytocompatibility of gel and its cell protection was tested postdirect injection by live and dead staining. 500  $\mu\text{L}$  mixture of live and dead staining was performed to count the number of cells with intact or damaged cells immediately postinjection.

**Long-Term Cell Viability Postsyringe Injection:** 100  $\mu\text{L}$  or 20  $\mu\text{L}$  of cells per hydrogel mixture with  $2.5 \times 10^6$  cells encapsulated were loaded on the corresponding hydrogel via the syringe injection and then cultured for 5 d following by the live and dead staining for cell viability.

**Live and Dead Staining:** Live and dead staining was performed to evaluate cell survival.  $0.5 \times 10^{-6}$  M Calcein AM and  $2 \times 10^{-6}$  M EthD-1 in per mL PBS were added in accordance with Life technology protocol. After 45 min of incubation at room temperature, samples were washed three times with PBS. Imaging was observed on fluorescent microscopy (Leica CTR6000) using LAS software to gather 5–10 randomly positioned images, and cell numbers were counted by Image J software.

**Microfluidic Velocity Measurement:** Simulated injections were conducted using a microfluidic setup. This allowed the visualization and quantification of the velocity profile of injected medium (PBS and our molecular Fmoc-Lam hydrogel) within the needle during administration.

Monodisperse polystyrene microspheres of diameter of 6  $\mu\text{m}$  were used as tracer particles. They were suspended within our molecular hydrogels and PBS at a concentration of  $2.10 \times 10^8$  particles  $\text{mL}^{-1}$ . To visualize dynamic flow, a 3D polydimethylsiloxane (PDMS) microfluidic chips was created with a simple straight channel (500  $\mu\text{m} \times 500 \mu\text{m} \times 16 \text{ mm}$ ) to mimic the size of injecting needle used for our cell transplantation study. The microfluidic chip was fabricated with 3D printed mold and PDMS.<sup>[46]</sup> The mold was designed using SketchUp 2015 software and printed by Up Mini 3d Printer (Tiertime) with acrylonitrile butadiene styrene (ABS) plastic filament. The transparent PDMS provided a clear imaging window to track the tracers using brightfield microscopy.

A syringe pump (KDS LEGATO 200) was used to provide constant injection velocity of 1  $\text{mL min}^{-1}$  for both the gel and PBS. A specialized high-speed charge-coupled device (CCD) camera (Point Grey Flea 3FL3-U3-13Y3M) was attached to an inverted microscopy (Leica DM IL LED) to capture the dynamic motion of microspheres in the channel during injection. A schematic diagram and the experimental setup showing the needle integrated within the microfluidic chip is shown (Figure S1, Supporting Information).

Motion blurring techniques were employed to track the fast-moving microspheres. The velocity of each sphere was calculated from single motion blurred image obtained from every frame.<sup>[47]</sup> The blurred trajectory represented the moving distance during camera exposure time. In this case, the microspheres were moving along a direction parallel to image plane of static camera. Therefore, the equation was simplified as velocity =  $(l_b - d_s)/ET$ , in which  $l_b$  is the length of blurred trace of the sphere and  $d_s$  is the diameter of the sphere. Measurements of microspheres within both the hydrogel and PBS were grouped by location (100  $\mu\text{m}$  interval) within the channel with a 25  $\mu\text{m}$  offset to correct for error in measurements, due to inability to measure within close proximally to the channel wall ( $\approx 25 \mu\text{m}$ ).

**Statistical Analysis:** All values are presented the mean  $\pm$  Standard Deviation (SD) of triplicate incubations. Data were analyzed by one-way analysis of variances (ANOVAs) with Turkey post-hoc tests using GraphPad Prism V6.0 (GraphPad, San Diego, CA, USA). Differences at  $P < 0.05$  were considered statistically significant. \*\*, \*\*\*, and \*\*\*\* represent  $P < 0.01$ ,  $P < 0.001$ , and  $P < 0.0001$ .

## Supporting Information

Supporting Information is available from the Wiley Online Library or from the author.

## Acknowledgements

D.N. and R.W. contributed equally to this work and Y.W. and X.H. are equal first author. This study was supported by funding from an ARC discovery project (DP130103131) and the NHMRC project (GNT1144996). Y.W. was supported by the Australian National University Student Ph.D. Scholarship (International) and X.F.H. was supported by a CSC-ANU PhD Scholarship; K.F.B. was supported by a Natural Sciences and Engineering Research Council of Canada (NSERC) Postgraduate Scholarship Doctoral (PGS D) award; B.G. was supported by RJL Hawke Fellowship from Australian Antarctic Division; A.T. was supported by a ARC DECRA (DE160100569) and Westpac2016 Research Fellowship; W.M.L. was supported by an ARC DECRA (DE160100843); and D.R.N. was supported by a NHMRC Dementia Research Leadership Fellowship (GNT1135687). Access to the facilities of the Centre for Advanced Microscopy (CAM) with funding through the Australian Microscopy and Microanalysis Research Facility (AMMRF) is gratefully acknowledged.

## Conflict of Interest

The authors declare no conflict of interest.

## Keywords

cell transplantation, dynamic self-assembly, hydrodynamic fluid model, microfluidic devices, molecular hydrogel

Received: January 13, 2019

Revised: November 7, 2019

Published online: December 19, 2019

- [1] a) M. M. Adil, A. T. Rao, G. N. Ramadoss, N. E. Chernavsky, R. U. Kulkarni, E. W. Miller, S. Kumar, D. V. Schaffer, *Adv. Funct. Mater.* **2018**, 28, 1804144; b) D. Joung, V. Truong, C. C. Neitzke, S. Z. Guo, P. J. Walsh, J. R. Monat, F. B. Meng, S. H. Park, J. R. Dutton, A. M. Parr, M. C. McAlpine, *Adv. Funct. Mater.* **2018**, 28, 1801850; c) L. J. Lu, Y. Wang, F. Zhang, M. W. Chen, B. L. Lin, X. H. Duan, M. H. Cao, C. S. Zheng, J. J. Mao, X. T. Shuai, J. Shen, *Adv. Funct. Mater.* **2018**, 28, 1706769.
- [2] D. W. Simon, M. J. McGeachy, H. Bayir, R. S. Clark, D. J. Loane, P. M. Kochanek, *Nat. Rev. Neurol.* **2017**, 13, 171.
- [3] L. R. Nih, S. Gojini, S. T. Carmichael, T. Segura, *Nat. Mater.* **2018**, 17, 642.
- [4] U. Dirnagl, C. Iadecola, M. A. Moskowitz, *Trends Neurosci.* **1999**, 22, 391.
- [5] a) R. A. Barker, M. Götz, M. Parmar, *Nature* **2018**, 557, 329; b) R. J. Nudo, *Front. Hum. Neurosci.* **2013**, 7, 887.
- [6] a) X. T. Hu, Z. Q. Huang, X. Zhou, P. W. Li, Y. Wang, Z. D. Huang, M. Su, W. J. Ren, F. Y. Li, M. Z. Li, Y. W. Chen, Y. L. Song, *Adv. Mater.* **2017**, 29, 1703236; b) Z. D. Huang, M. Su, Q. Yang, Z. Li, S. R. Chen, Y. F. Li, X. Zhou, F. Y. Li, Y. L. Song, *Nat. Commun.* **2017**, 8, 14110; c) M. Su, Z. D. Huang, Y. F. Li, X. Qian, Z. Li, X. T. Hu, Q. Pan, F. Y. Li, L. H. Li, Y. L. Song, *Adv. Mater.* **2018**, 30, 1703963.
- [7] a) G. Orive, E. Anitua, J. L. Pedraz, D. F. Emerich, *Nat. Rev. Neurosci.* **2009**, 10, 682; b) A. K. A. Silva, S. Perretta, G. Perrod, L. Pidial, V. Lindner, F. Carn, S. Lemieux, D. Alloeyau, I. Boucenna, P. Menasche, B. Dallemagne, F. Gazeau, C. Wilhelm, C. Cellier, O. Clement, G. Rahmi, *ACS Nano* **2018**, 12, 9800; c) L. Cai, R. E. Dewi, A. B. Goldstone, J. E. Cohen, A. N. Steele, Y. J. Woo, S. C. Heilshorn, *Adv. Healthcare Mater.* **2016**, 5, 2758.
- [8] J. G. Zhang, C. Cheng, J. L. Cuellar-Camacho, M. J. Li, Y. Xia, W. Z. Li, R. Haag, *Adv. Funct. Mater.* **2018**, 28.

- [9] a) C. M. Madl, S. C. Heilshorn, *Annu. Rev. Biomed. Eng.* **2018**, *20*, 21; b) M. B. Rahmany, M. Van Dyke, *Acta Biomater.* **2013**, *9*, 5431; c) C. M. Madl, S. C. Heilshorn, H. M. Blau, *Nature* **2018**, 557, 335.
- [10] a) J. G. Hunsberger, M. Rao, J. Kurtzberg, J. W. Bulte, A. Atala, F. M. LaFerla, H. T. Greely, A. Sawa, S. Gandy, L. S. Schneider, *Lancet Neurol.* **2016**, *15*, 219; b) R. A. Barker, M. Parmar, L. Studer, J. Takahashi, *Cell Stem Cell* **2017**, *21*, 569; c) J. P. A. Ioannidis, B. Y. S. Kim, A. Trounson, *Nat. Biomed. Eng.* **2018**, *2*, 797.
- [11] C. Winkler, D. Kirik, A. Björklund, *Trends Neurosci.* **2005**, *28*, 86.
- [12] R. A. Barker, J. Barrett, S. L. Mason, A. Björklund, *Lancet Neurol.* **2013**, *12*, 84.
- [13] R. A. Barker, J. Drouin-Ouellet, M. Parmar, *Nat. Rev. Neurol.* **2015**, *11*, 492.
- [14] a) B. D. Olsen, J. A. Kornfield, D. A. Tirrell, *Macromolecules* **2010**, *43*, 9094; b) B. A. Aguado, W. Mulyasmita, J. Su, K. J. Lampe, S. C. Heilshorn, *Tissue Eng., Part A* **2012**, *18*, 806.
- [15] Y. Chisti, *Crit. Rev. Biotechnol.* **2001**, *21*, 67.
- [16] a) J. H. Wen, L. G. Vincent, A. Fuhrmann, Y. S. Choi, K. C. Hribar, H. Taylor-Weiner, S. Chen, A. J. Engler, *Nat. Mater.* **2014**, *13*, 979; b) J. Lou, F. Liu, C. D. Lindsay, O. Chaudhuri, S. C. Heilshorn, Y. Xia, *Adv. Mater.* **2018**, *30*, 1705215; c) A. A. Foster, R. E. Dewi, L. Cai, L. Hou, Z. Strassberg, C. A. Alcazar, S. C. Heilshorn, N. F. Huang, *Biomater. Sci.* **2018**, *6*, 614; d) L. Cai, R. E. Dewi, S. C. Heilshorn, *Adv. Funct. Mater.* **2015**, *25*, 1344.
- [17] a) J. L. Drury, D. J. Mooney, *Biomaterials* **2003**, *24*, 4337; b) L. T. Saldin, M. C. Cramer, S. S. Velankar, L. J. White, S. F. Badylak, *Acta Biomater.* **2017**, *49*, 1; c) R. Sridhar, R. Lakshminarayanan, K. Madhaiyan, V. A. Barathi, K. H. C. Lim, S. Ramakrishna, *Chem. Soc. Rev.* **2015**, *44*, 790; d) C. M. Madl, L. M. Katz, S. C. Heilshorn, *Adv. Funct. Mater.* **2016**, *26*, 3612.
- [18] L. Haines-Butterick, K. Rajagopal, M. Branco, D. Salick, R. Rughani, M. Pilarz, M. S. Lamm, D. J. Pochan, J. P. Schneider, *Proc. Natl. Acad. Sci. USA* **2007**, *104*, 7791.
- [19] K. T. Nguyen, J. L. West, *Biomaterials* **2002**, *23*, 4307.
- [20] Y. S. Zhang, A. Khademhosseini, *Science* **2017**, *356*, eaaf3627.
- [21] D. R. Nisbet, A. E. Rodda, M. K. Horne, J. S. Forsythe, D. I. Finkelstein, *Tissue Eng., Part A* **2010**, *16*, 2833.
- [22] A. L. Rodriguez, C. L. Parish, D. R. Nisbet, R. J. Williams, *Soft Matter* **2013**, *9*, 3915.
- [23] a) F. A. Soma, T.-Y. Wang, J. C. Niclis, K. F. Bruggeman, J. A. Kauhausen, H. Guo, S. McDougall, R. J. Williams, D. R. Nisbet, L. H. Thompson, *Cell Rep.* **2017**, *20*, 1964; b) D. Nisbet, T. Wang, K. Bruggeman, J. Niclis, F. Soma, V. Penna, C. Hunt, Y. Wang, J. Kauhausen, R. Williams, *Adv. Biosyst.* **2018**, *2*, 1800113.
- [24] C. C. Horgan, A. L. Rodriguez, R. Li, K. F. Bruggeman, N. Stupka, J. K. Raynes, L. Day, J. W. White, R. J. Williams, D. R. Nisbet, *Acta Biomater.* **2016**, *38*, 11.
- [25] A. Faissner, J. Reinhard, *Glia* **2015**, *63*, 1330.
- [26] U. Theodoridis, K. Long, C. French-Constant, A. Faissner, *Prog. Brain Res.* **2014**, *214*, 3.
- [27] J. Wang, L. Yin, Z. Chen, *Neural Regener. Res.* **2013**, *8*, 376.
- [28] D. Bonneh-Barkay, C. A. Wiley, *Brain Pathol.* **2009**, *19*, 573.
- [29] A. M. Smith, R. J. Williams, C. Tang, P. Coppo, R. F. Collins, M. L. Turner, A. Saiani, R. V. Ulijn, *Adv. Mater.* **2008**, *20*, 37.
- [30] K. Tao, A. Levin, L. Adler-Abramovich, E. Gazit, *Chem. Soc. Rev.* **2016**, *45*, 3935.
- [31] Y. Li, J. Chen, L. Wang, M. Lu, M. Chopp, *Neurology* **2001**, *56*, 1666.
- [32] K. Tashiro, G. C. Sephel, B. Weeks, M. Sasaki, G. R. Martin, H. K. Kleinman, Y. Yamada, *J. Biol. Chem.* **1989**, *264*, 16174.
- [33] G. A. Silva, C. Czeisler, K. L. Niece, E. Beniash, D. A. Harrington, J. A. Kessler, S. I. Stupp, *Science* **2004**, *303*, 1352.
- [34] a) G. T. Eisenhoffer, P. D. Loftus, M. Yoshigi, H. Otsuna, C. B. Chien, P. A. Morcos, J. Rosenblatt, *Nature* **2012**, *484*, 546; b) R. Levayer, C. Dupont, E. Moreno, *Curr. Biol.* **2016**, *26*, 670; c) E. Marinari, A. Mehonic, S. Curran, J. Gale, T. Duke, B. Baum, *Nature* **2012**, *484*, 542.
- [35] F. L. Maclean, G. M. Ims, M. K. Horne, R. J. Williams, D. R. Nisbet, *Adv. Mater.* **2018**, *30*, e1805209.
- [36] A. L. Rodriguez, T. Y. Wang, K. F. Bruggeman, C. C. Horgan, R. Li, R. J. Williams, C. L. Parish, D. R. Nisbet, *J. Mater. Chem. B* **2014**, *2*, 7771.
- [37] S. Kaech, G. Banker, *Nat. Protoc.* **2006**, *1*, 2406.
- [38] E. J. Huang, L. F. Reichardt, *Annu. Rev. Neurosci.* **2001**, *24*, 677.
- [39] C. Yan, A. Altunbas, T. Yucel, R. P. Nagarkar, J. P. Schneider, D. J. Pochan, *Soft Matter* **2010**, *6*, 5143.
- [40] E. L. Bakota, Y. Wang, F. R. Danesh, J. D. Hartgerink, *Biomacromolecules* **2011**, *12*, 1651.
- [41] M. Wang, L. Z. Hu, C. J. Xu, *Lab Chip* **2017**, *17*, 1373.
- [42] V. N. Modepalli, A. L. Rodriguez, R. Li, S. Pavuluri, K. R. Nicholas, C. J. Barrow, D. R. Nisbet, R. J. Williams, *Biopolymers* **2014**, *102*, 197.
- [43] R. J. Williams, T. E. Hall, V. Glattau, J. White, P. J. Pasic, A. B. Sorensen, L. Waddington, K. M. McLean, P. D. Currie, P. G. Hartley, *Biomaterials* **2011**, *32*, 5304.
- [44] R. Li, N. L. McRae, D. R. McCulloch, M. Boyd-Moss, C. J. Barrow, D. R. Nisbet, N. Stupka, R. J. Williams, *Biomacromolecules* **2018**, *19*, 825.
- [45] D. Nisbet, S. Pattanawong, N. Ritchie, W. Shen, D. Finkelstein, M. K. Horne, J. S. Forsythe, *J. Neural Eng.* **2007**, *4*, 35.
- [46] a) J. Friend, L. Yeo, *Biomicrofluidics* **2010**, *4*, 026502; b) M. Villegas, Z. Cetinic, A. Shakeri, T. F. Didar, *Anal. Chim. Acta* **2018**, *1000*, 248.
- [47] H.-Y. Lin, K.-J. Li, C.-H. Chang, *Image Vision Comput.* **2008**, *26*, 1327.
- [48] A. L. Rodriguez, T.-Y. Wang, K. F. Bruggeman, R. Li, R. J. Williams, C. L. Parish, D. R. Nisbet, *Nano Res.* **2015**, *9*, 674.
- [49] S. M. Kelly, T. J. Jess, N. C. Price, *Biochim Biophys Acta (BBA) - Proteins Proteomics* **2005**, *1751*, 119.